Journal of Applied Electrochemistry
https://doi.org/10.1007/s10800-020-01493-2

RESEARCH ARTICLE

A novel nano-YSZ-Al alloy anode for Al–air battery

Siva Palanisamy[1] · Naveenkumar Rajendhran[2] · Surendhiran Srinivasan[2] · Arunkumar Prabhakaran Shyma[2] · Vinoth Murugan[3] · Bhoopathy Parasuraman[4] · Soorathep Kheawhom[1,5]

Received: 29 April 2020 / Accepted: 10 October 2020

Abstract

Recently, aluminium–air batteries have received great attention because of their high specific capacity and low cost. However, corrosion of the aluminium (Al) anode is a critical problem limiting their practical applications. In this study, a decrease in the corrosion and an increase in the discharge performance of the Al anode were demonstrated through the use of nano-yttrium-stabilized zirconium (nano-YSZ). Three weight ratios of nano-YSZ blended with Al were prepared via mechanical stir casting. The surface hardness of the new Al alloys was determined using nano-indentation method and phase transition. Crystallite size measurements were conducted using X-ray diffraction analysis. Subsurface morphologies were conducted using scanning electron microscopy. Corrosion studies were carried out using electrochemical impedance spectroscopy and linear sweep voltammetry. The discharge and short-circuit studies of the prepared Al–air battery were undertaken using different Al alloy anodes. The results demonstrated that the Al anode having a higher ratio of nano-YSZ (5 wt%) had the highest discharge behaviour and excellent corrosion resistance making it a potential candidate as an electrode for the Al–air battery.

Siva Palanisamy and Naveenkumar Rajendhran contributed equally to this study.

✉ Siva Palanisamy
sivachemist88@gmail.com

✉ Soorathep Kheawhom
soorathep.k@chula.ac.th

[1] Department of Chemical Engineering, Faculty of Engineering, Chulalongkorn University, Bangkok 10330, Thailand

[2] Centre for Nano Science and Technology, K.S. Rangasamy College of Technology, Tiruchengode, Tamil Nadu 637 215, India

[3] Department of Electrical and Electronics Engineering, Selvam College of Technology, Namakkal, Tamil Nadu 637003, India

[4] Department of Chemistry, Vivekananda College of Arts and Science for Women, Tiruchengode, Tamil Nadu 637 205, India

[5] Research Unit of Advanced Materials for Energy Storage, Chulalongkorn University, Bangkok 10330, Thailand

Published online: 02 November 2020

Graphic abstract

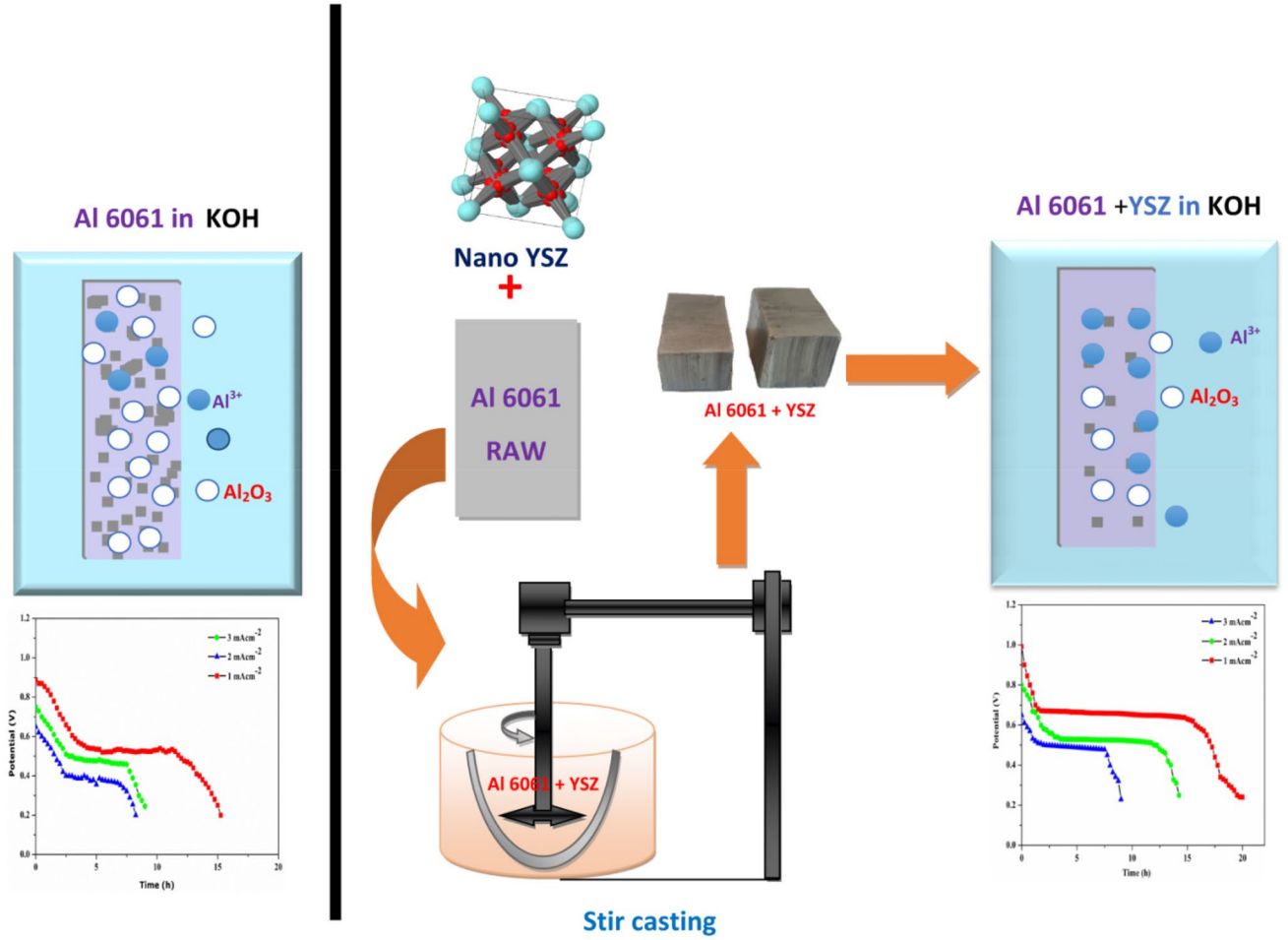

Keywords Nano-yttrium-stabilized zirconium · Air battery · Nano-indentation · Aluminium alloys · Mechanical stir casting

1 Introduction

Recent studies on the use of anode materials for metal–air batteries focus on materials such as lithium (Li), aluminium (Al), zinc (Zn) and magnesium (Mg) [1–4]. A metal anode acts as fuel in the battery system. The selection of proper metal or metal alloys to serve as an anode plays a vital role in enhancing battery performance [5–8]. Al can be easily recycled in a metal–air battery compared to any other anode material [9]. Both the theoretical capacity and cell voltage of Al are 8046 mAh cm^{-3} and 2.4 V, respectively, which are higher than those of other metals used in air batteries [9, 10]. The volumetric capacity of an Al anode is 8.0 Ah cm^{-3}, which is four times higher than that of a Li anode, i.e. 2.0 Ah cm^{-3}. Gravimetric capacity can also be compared: 2.0 Ah g^{-1} for Al and 3.9 Ah g^{-1} for Li [11]. This is the only practical battery based on a trivalent charge carrier, which means that each ion transfer is accompanied by three times more charge storage than Li-ion batteries (LIBs) [12, 13]. On the one hand, a metallic anode consisting of Al or Mg is not an issue due to their appropriate chemical reactivity [11]. On the other hand, Al or Al alloys are ideal metal anode materials, considering their availability and cost-effectiveness [12, 13]. The performance of Al–air batteries and their discharge capacities are shown in Table 1 [14–18].

Pure Al has excellent electrochemical properties although it is unstable when used as an anode for an Al–air battery. A pure Al electrode in aqueous electrolytes causes corrosion and passivation of the surface of Al due to side reaction (Al_2O_3 and $Al(OH)_3$), which is the major limitation of pure Al–air batteries [11]. Certain methods such as changing the composition of the alloying elements and applying electrolyte additives are used to limit corrosion.

Table 1 Different Al–air batteries: discharge capacities

Electrode	Performance/remarks	Reference
Al	Capacity 105 mAh g^{-1}, Power density 5.5 mW cm^{-2}, Higher KOH concentration decreases the cell capacity.	[14]
Al alloys	Capacity 426 mAh g^{-1}	[15]
Al alloys	Capacity 2590 Ah consist of 10 cells, Power density 577 Wh kg^{-1}, High capacity due to Ga-Sn-Mg alloying	[16]
Al	Capacity 1166 mAh g^{-1}, PAA gel delivered high conductivity nearly equal to aqueous electrolytes.	[17]
Al	Capacity 800 mAh g^{-1}, Anhydrous hydroxide ion conducting electrolyte	[18]

Experimentally done delithiation of different Li_xSi surfaces has determined that delithiation generally occurs at higher voltages than does the initial lithiation [19]. Li_xO and Li_ySi forms having an increasing concentration of Li make a major contribution to the capacity of SiCO. In essence, the high carbon content of SiCO has a larger lithium capacity as an anode of a Li-ion battery [20–22].

The most commonly used Al alloys, namely, Al–Zn, Al–In, Al–Ga and Al–Sn show enhanced battery operation time with a decrease in the corrosion rate when applied in air batteries [12]. The combination of Al-6061/ZrO_2 results in excellent corrosion resistance in aqueous electrolytes [13]. Nano-YSZ shows excellent properties such as high mechanical strength, good chemical stability, high level of oxygen-ion conductivity, corrosion resistance and low thermal conductivity [24–28]. The reinforcement of nano-YSZ in the Al matrix and macro-sized YSZ is reported elsewhere [29]. Although YSZ-Al alloy offers significant benefits, it has not been applied as the anode for an Al–air battery.

In this study, an Al anode material is developed using three different weight ratios, i.e. nano-YSZ (2.5, 3.5 and 5 wt%), blended with Al-6061 via mechanical stir casting. The synthesized alloys have been comprehensively characterized to explore their discharge behaviour in the Al–air battery.

2 Materials and methods

2.1 Materials

In this study, AR-grade chemicals procured from Merck, India, were used without any additional purification. The solutions were prepared using double-distilled (DD) water (pH 6.99) purified through Milli-Q Ultrapure Water System (6110F; Merck, Germany). The materials used in this study such as O_2 permeable hydrophobic Teflon film, stainless-steel (SS304) mesh with a pore size of 1 mm, an acrylic sheet (100 mm × 100 mm) and an aluminium sheet (Al-6061) were obtained from Chemico (India).

2.2 Synthesis of nano-YSZ

A large-scale 8 wt% nano-YSZ powder was prepared by the Pechini process. The AR-grade materials such as zirconium oxychloride hexahydrate ($ZrOCl_2{\cdot}6H_2O$; 99% pure), yttrium nitrate hexahydrate ($Y(NO_3)_3{\cdot}6H_2O$; 99% pure), citric acid monohydrate ($C_6H_8O_7{\cdot}H_2O$; 99% pure) and ethylene glycol (EG) (all from SRL, India) were used as precursors for this process. First, zirconium oxychloride and yttrium nitrate were taken in two distinct beakers and dissolved in DD water under continuous stirring at 60 °C to obtain perfect dilution.

Next, the obtained solutions were transferred into one beaker and continuously stirred at 60 °C. In this process, both the overall weight ratio of Y_2O_3/ZrO_2 and their stabilization were maintained at 8:92 (8 wt% YSZ) to prepare citric acid. The prepared citric acid was added to the precursors after homogenization of the solution with a molar ratio of 4:1. For the esterification process, the solution was again mixed with EG at 1:1 ratio. Then, the obtained viscous solution was continuously stirred at 80 °C for 12 h giving rise to a gel-like formation. Finally, the gel was heat treated for 2 h at 1000 °C using a hot-air oven. The obtained precipitates (Y_2O_3–ZrO_2) were carefully collected after the heat treatment and used for further characterization [30].

2.3 Stir casting

Stir casting is one of the commercial casting techniques used to blend nanocrystalline powders with the Al matrix alloy at different concentrations: 2.5, 3.5 and 5 wt% of nano-YSZ. The optimum lower (2.5 wt%) and higher (5 wt%) concentrations of nano-YSZ additive in this investigation were considered on the basis of earlier studies [13]. The as-synthesized nano-YSZ powder was initially preheated up to 300 °C for 30 min. During this process, Al-6061 was used as a base metal, hereafter termed as Al.

The base metal was melted at 600 °C in a graphite crucible, after which the melted Al was stirred at higher temperatures of 800–900 °C. During the process of stirring, the prepared nano-YSZ powder, as an inoculant, was slowly added. Thereafter, the prepared molten metal was poured into a readymade die to obtain the required shape. Then, the

prepared composite is solidified and separated from the die. The experiment was conducted at three concentrations: 2.5, 3.5 and 5 wt% of nano-YSZ. The prepared casting alloys, which contained different additives viz. 2.5, 3.5 and 5 wt% nano-YSZ are hereafter termed as Al-1, Al-2 and Al-3, respectively.

2.4 Al–air battery construction

A rectangular acrylic sheet was used to construct the Al–air battery. The prepared alloys, namely, Al-1, Al-2 and Al-3 were used as an anode and compared with Al, whereas SS304 grade SS mesh with an air-exposed area of 10 cm^2 was used as an oxygen electrode. Electrolyte leakage was prevented using air-permeable Teflon film. In Fig. 1, the image of the prepared Al–air battery cell is shown. The electrochemical studies of the constructed Al–air batteries were performed in 1 M potassium hydroxide (KOH) electrolyte.

2.5 Characterization

The phase and structure of Al, Al-1, Al-2 and Al-3 plates were analysed using an X-ray diffractometer (X'Pert PRO; PANalytical, the Netherlands) using CuKα ($\lambda = 1.5406$ Å) as a source of radiation. The surface hardness values of Al, Al-1, Al-2 and Al-3 plates were analysed using a nano-indenter (Ti 700 Ubi 1; Hysitron, USA). Both the operating life and the discharge current of the constructed Al, Al-1, Al-2 and Al-3–air batteries were examined for the discharge current densities of 1, 2 and 3 mA cm^{-2}. The discharge voltage and current were monitored until 0.2 V, at a regular interval of 5 min. The performance of the battery under short-circuit conditions was also tested. The surface and subsurface morphologies of the samples were recorded via a scanning electron microscope (JSM-6390LV; SEM, Japan) at 20 kV with a magnification of 10,000× at 1-μm scale.

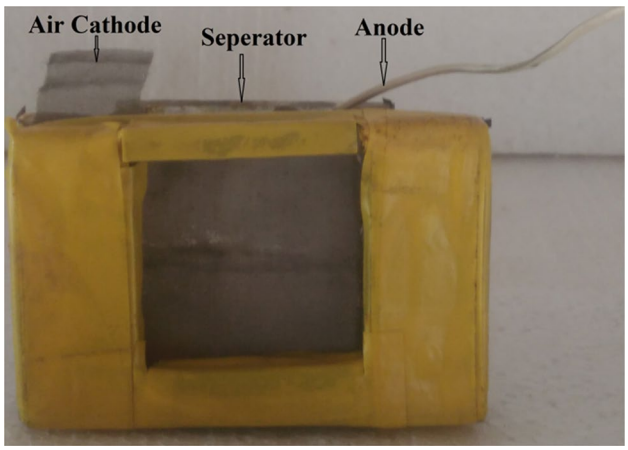

Fig. 1 Schematic representation of the prepared Al–air battery cell

The Raman spectra of the samples were obtained using the LabRAHMR-800 (HORIBA, France) spectrometer. The corrosion behaviour of the anode and EIS were carried out using a three-electrode setup. An electrical potential between 1.2 and 0.1 V at an amplitude of 100 mV over the frequency range from 0.01 Hz to 1 MHz was applied to carry out EIS studies using an electrochemical workstation (PGSTAT302N; Metrohm Autolab, the Netherlands) at room temperature. The Al, Al-1, Al-2 and Al-3 plates were subsequently polished with 9-mm, 3-mm and 1-mm silicon carbide grit papers and cleaned after each step with acetone and distilled water. The polished plates were dried in a hot-air oven at 353 K for 1 h and then used for corrosion studies. The applied potential or potential window for corrosion study was − 1.7 to − 1.4 V at a scanning rate of 5 mV. Corrosion potential (V_{corr}) and corrosion current (i_{corr}) were determined from the extrapolated data of the cathodic and anodic parts of the potentiodynamic polarization study or Tafel plot.

3 Results and discussion

The nanoparticles were in narrow size distribution, as shown by the scanning electron microscopy (SEM) image in Fig. 2a. Moreover, the observed SEM image shows a fine morphology with smaller nanoparticle sizes. Figure 2b shows various X-ray diffraction (XRD) patterns of the as-synthesized nano-YSZ powder. The 2θ values of XRD peaks indexed at 30°, 34.5°, 49.9°, 59.3°, 62.1° and 73.2° corresponding to (111), (200), (220), (311), (222) and (400) planes match with the JCPDS standard card number 48-0224 [31–33]. The XRD results confirm the characteristic reflection and diffraction patterns of YSZ in its tetragonal phase, as reported earlier [34–36]. The absence of additional peaks in the XRD pattern shows that Y_2O_3 is completely stabilized in the zirconia dioxide (ZrO_2) lattice. The average crystallite size was calculated using the following Scherrer formula [37–39]:

$$D = \frac{0.9\lambda}{\mathrm{FWHM}\cos\theta} \quad (1)$$

where D is the average crystallite size, λ is the wavelength of X-ray, θ is the diffraction angle and FWHM is the full width at the half maximum of X-ray peaks appearing at the diffraction angle θ. The calculated average crystallite size of YSZ nanocrystalline powder was 7.54 nm.

Raman spectroscopy is a more appropriate technique to study different modifications of the stabilized zirconia crystal structure due to its high sensitivity of Raman scattering to both intermediate periodicity and oxygen displacement compared to the XRD method [37]. On the basis of group theory, the Raman active modes of cubic, tetragonal and

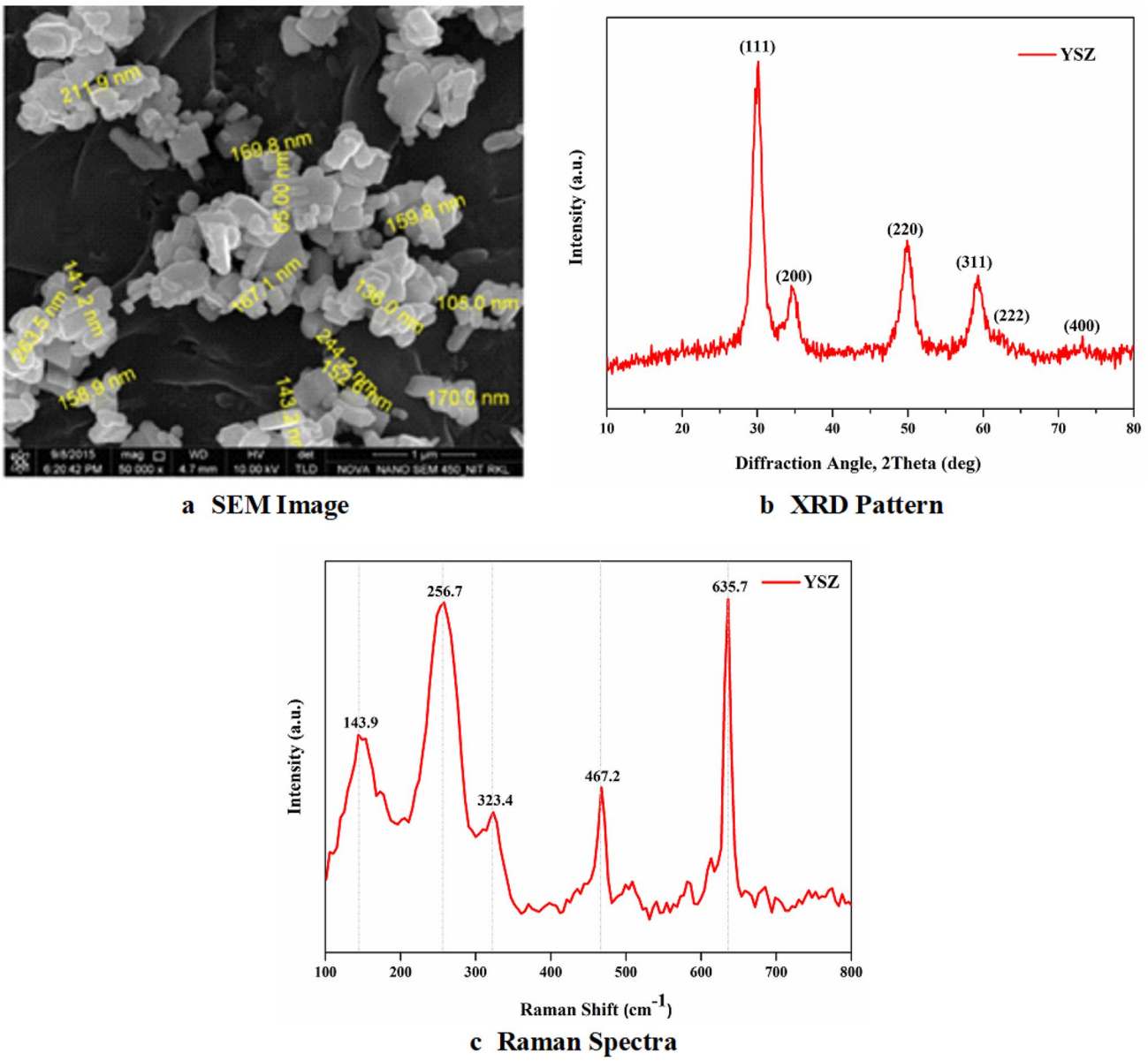

Fig. 2 **a** SEM image, **b** XRD pattern and **c** Raman spectra of YSZ

monoclinic phases of zirconia are expected to have 1T 2 g, $6(1A_{1g}+2B_{1g}+3E_g)$ and 18 $(9A_g+9B_g)$, respectively [37, 38]. Figure 2c shows typical Raman spectra of the as-synthesized nano-YSZ. The peaks observed at 143.9, 256.7, 323.4, 467.2 and 635.7 cm^{-1} correspond to E_g, E_g, B_g, E_g and A_g modes, respectively, which confirm the tetragonal phase of the obtained nano-YSZ [41, 42]. The observed result is in line with the confirmation of X-ray analysis (Fig. 2b).

Figure 3 displays low-magnification SEM images of surface morphology and cross section of Al-1, Al-2 and Al-3. These results revealed that in all cases, YSZ particles were distributed uniformly in the Al matrix, indicating an excellent interfacial bonding between YSZ particles and the Al matrix. Only a small fraction of agglomerated YSZ particles was observed on the matrix.

Figure 4a shows the XRD patterns of Al-6061 and three YSZ weight ratios present in the Al alloys: namely, Al-1, Al-2 and Al-3. The XRD patterns of the starting specimen (Al-6061 plate) and Al alloys are depicted with diffraction peaks at 39° for (111), 44° for (200), 66° for (220) and 78° for (311) planes (JCPDS card no. 04-0787), indicating the presence of Al [43]. The XRD patterns of Al-3 clearly indicate YSZ peaks indexed at 30°, 34°, 49°, 59°, 62° and 73° corresponding to (111), (200), (220), (311), (222) and (400) planes, respectively, compared to those of other composites such as Al-1 and Al-2.

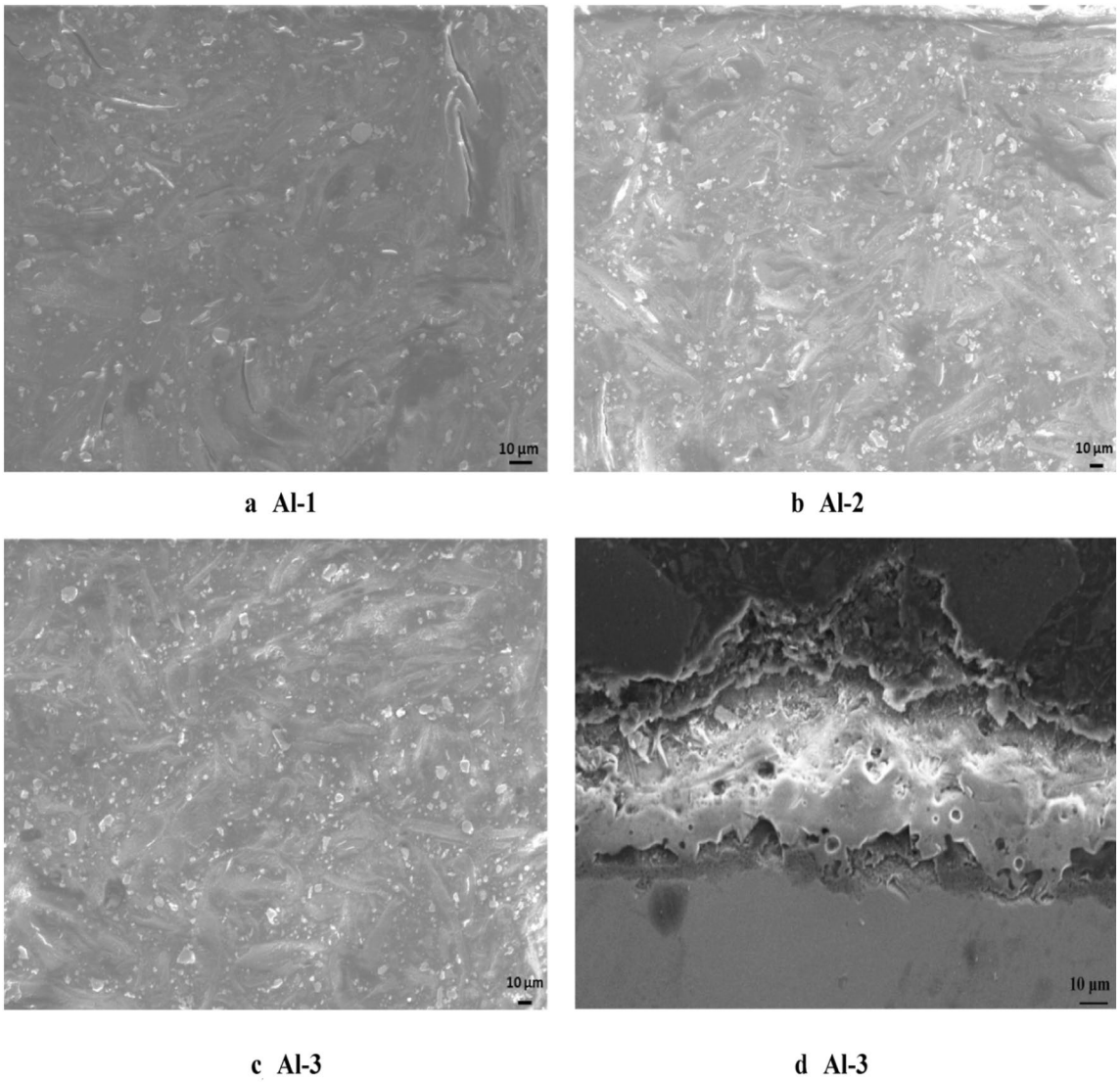

Fig. 3 Low-magnification SEM images of **a** Al-1, **b** Al-2, **c** Al-3 and **d** Al-3

As electrochemical reactions occur only on the electrode surface, an electrochemical property is oriented with the mechanical property of the electrodes and it is closely connected to the surface layer of the electrode [44]. In order to understand the electrochemical responses of the electrode surface because of the mechanical modification, an appropriate technique such as nano-indentation can be used. Nano-indentation affords a good approach for this intention. The surface morphology of the Al-6061 metal plate and its Al alloys were studied using nano-indentation.

Surface roughness and hardness are important properties to avoid electrochemical damage happening. The typical load–indentation depth curves for the Al-6061 metal plate and its Al alloys are shown in Fig. 4b. In Fig. 4, the load/unload curves for the entire specimen without the alloy Al metal plate show greater indentation depth than the other alloy Al metal plates. An increase in the weight concentration of YSZ leads to a decrease in the indentation depth, particularly at 5 wt% YSZ; the Al metal plate (Al-3) shows very low indentation depth. Figure 5 shows the hardness values of Al-6061 and Al alloy plates using a 3D surface topography. The change in the surface morphology of the Al-6061 alloy shows the changes taking place during the alloying treatment with the nano-YSZ. The hardness of the metal surface increases with the addition of nano-YSZ [45]. In the case of Al-3, the surface hardness is higher than that of Al, Al-1 and Al-2. The increase in the surface hardness of the Al alloys is in line with the increase in crystallite size (Table 2).

The discharge performances of the Al–air batteries for the four Al electrodes in 1 M aqueous KOH electrolytes

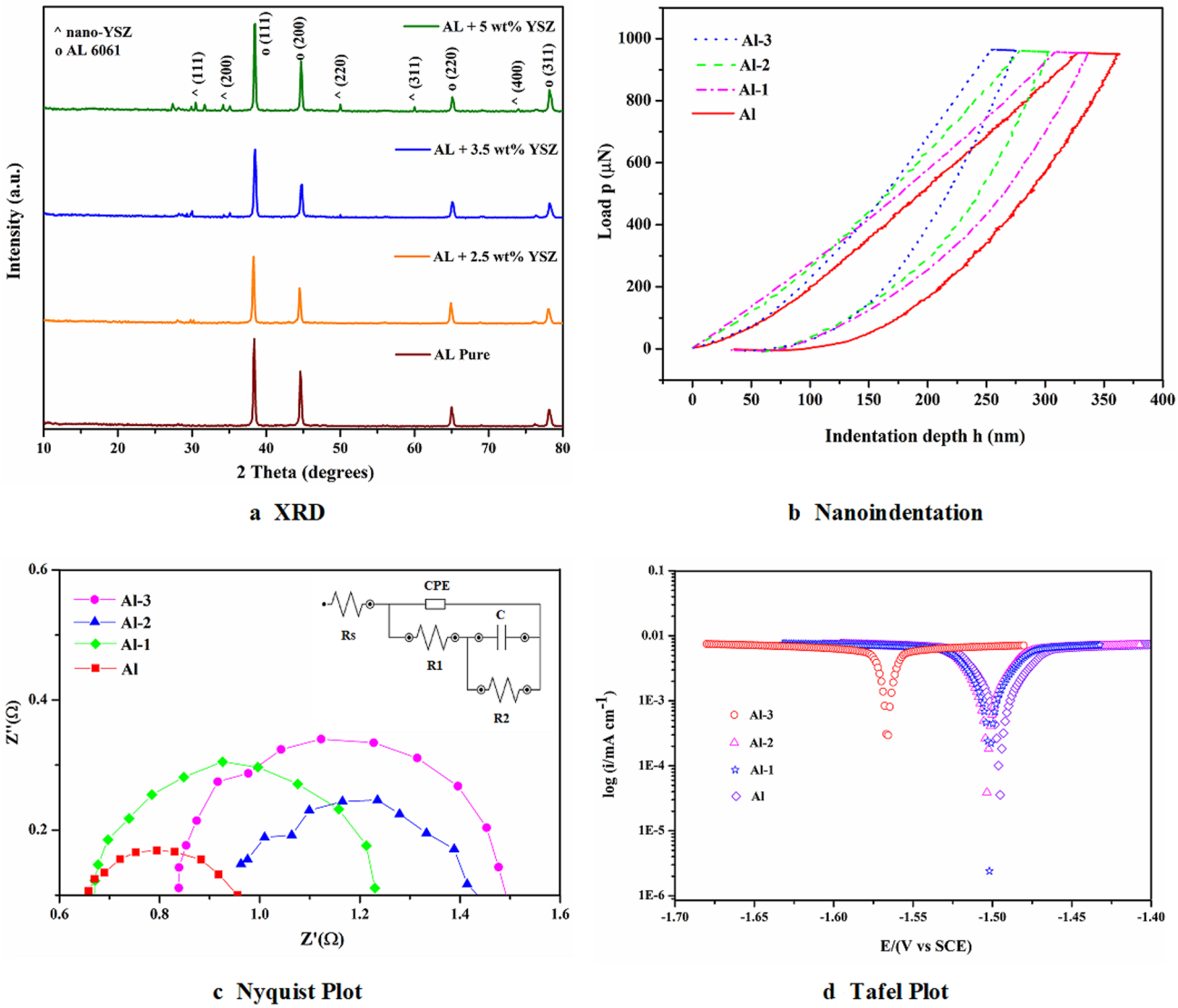

Fig. 4 **a** XRD patterns, **b** Nano-indentation load/unload curves, **c** Nyquist plots, **d** Tafel plots of Al-6061 and YSZ-Al alloys

obtained for the three current densities, i.e. 1, 2 and 3 mA cm^{-2}, are shown in Figs. 6a–d, respectively.

Battery discharge performance was determined by plotting current densities under various load conditions rather than the total battery drain current. The operating life of the battery in hours was determined using the discharge current data. In addition to the above variable load conditions, the Al–air battery was tested further under short-circuit condition [5]. The short-circuit studies of the prepared air batteries using different alloy formulations are given in Table 3.

The different weight percentages of nano-YSZ added with Al(6061) alloy greatly improved anode performance, as shown in Fig. 5. The prevention of self-corrosion by nano-YSZ can be a reason behind the increased efficiency of the constructed battery that uses nano-YSZ-added anodes. The Al-3 alloy demonstrates 31%, 58% and 9% higher discharge lifetime compared to Al-2 (21%, 33% and 6%) and Al-1 (17%, 13% and 12%) in comparison to the bare Al electrode at 1, 2 and 3 mA cm^{-2}. These results suggest that the higher alloying percentage of YSZ with the Al plate yields higher shelf life for the constructed battery (Al-3 alloy anode). When a high discharge current density is 3mAhcm^{-2} at air battery, the active material is restricted by a slower electrode kinetics. So the discharge life becomes smaller as a consequence [46].

The EIS shown in Fig. 4c and inset demonstrate the electrical equivalent circuit model of the reaction process. In the EIS diagram, a semicircle was attained at low frequencies (from 0.83 to 1.49 Hz), which is linearly related to the charge transfer resistance of the reaction (associated with the corrosion process). R1 is the charge transfer resistance value, attained from the arc of the semicircle at low frequencies;

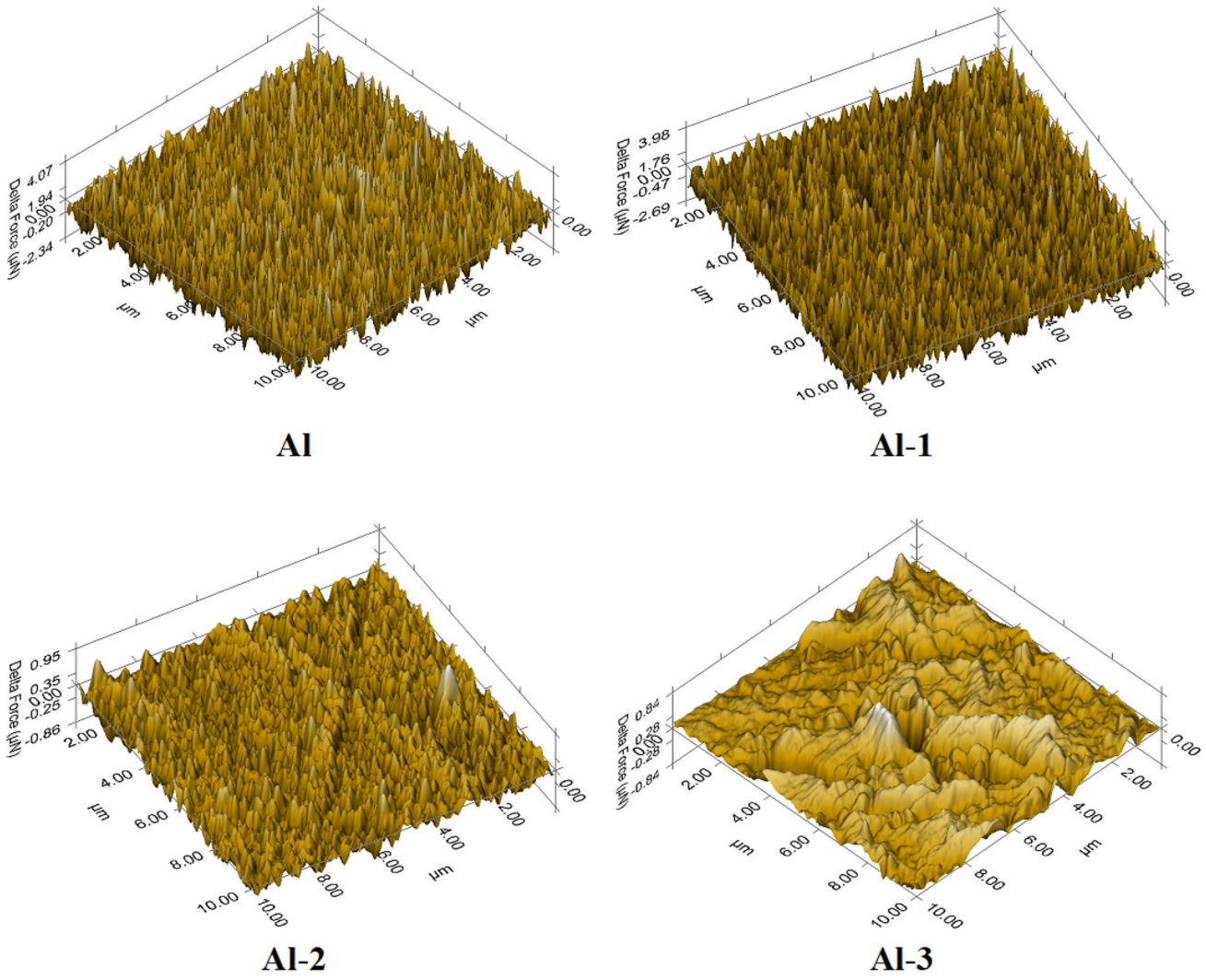

Fig. 5 3D surface topographies of Al-6061 and YSZ-Al alloys

Table 2 Capacity, crystallite size and hardness of Al-6061 and YSZ-Al alloys

Processing condition	Current density (mA cm^{-1})	Open-circuit voltage (V)	Discharge time (h)	Capacity (mA hg^{-1})	Crystallite size (nm)	Hardness (MPa) (±0.32)
Al	1	1. 41	15.25	462	32.99	817.85
	2	1. 41	09.00	582		
	3	1. 41	8.25	720		
Al-1	1	1. 42	16.50	510	34.25	851.00
	2	1. 42	10.75	648		
	3	1. 42	08.50	756		
Al-2	1	1. 43	17.00	519	35. 49	969. 20
	2	1. 43	12.25	756		
	3	1.43	08.00	684		
Al-3	1	1. 44	20.00	600	36. 99	1030.0
	2	1. 44	14.25	882		
	3	1. 44	09.00	810		

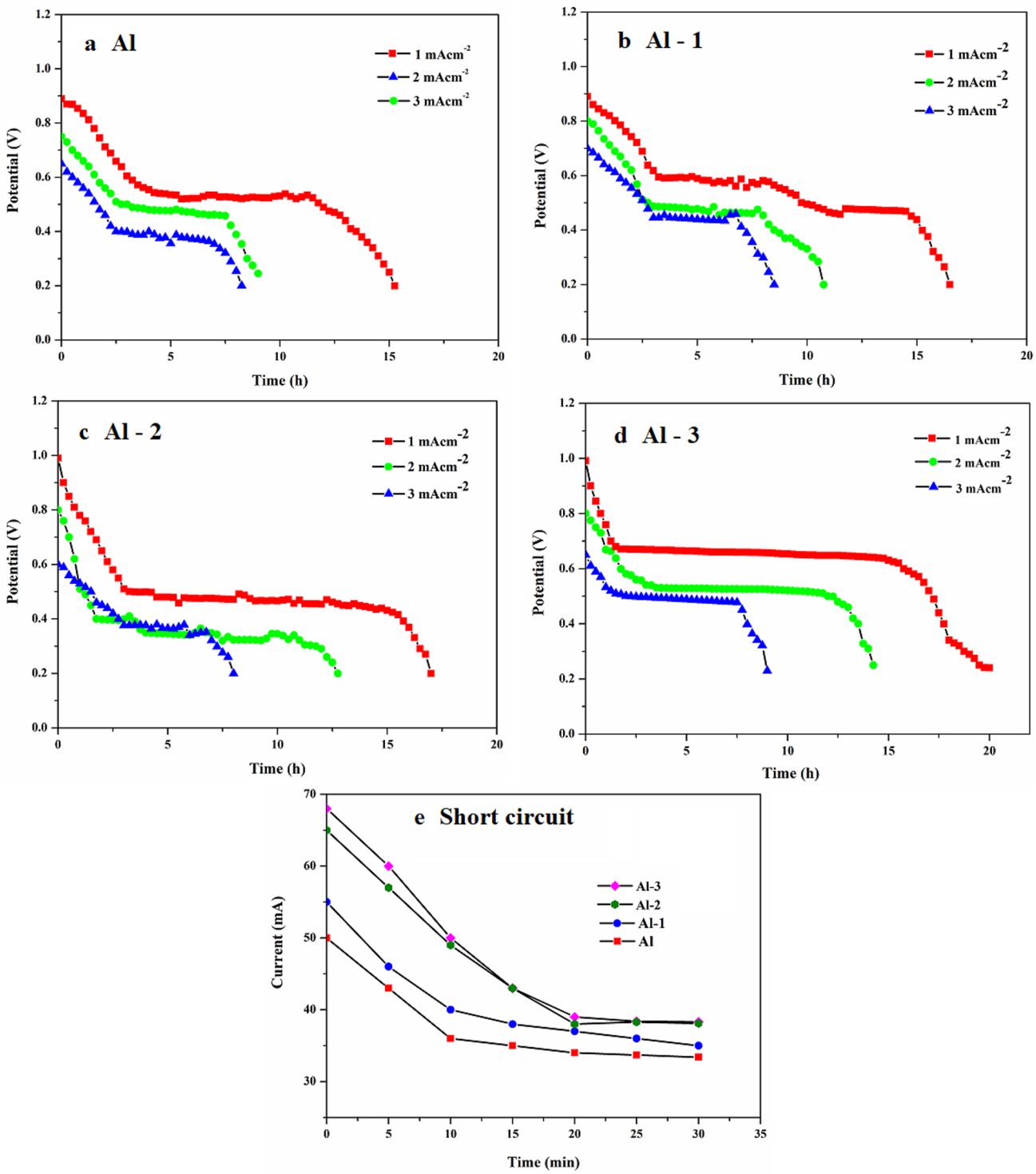

Fig. 6 Discharge and short-circuit studies of Al-6061 and YSZ-Al alloys

it is directly proportional to the material's corrosion resistance. The R1 value and corrosion resistance are very high for Al-1 and Al-3 and are greater than Al. The R1 value steadily increases with the increase in the ratio of nano-YSZ in the Al alloy. From the results achieved, it is clear that the addition of nano-YSZ in the Al alloy can enhance its corrosion resistance; resistance to corrosion can also be enhanced with the increase in concentration levels [47].

In Fig. 4d, Tafel plots were used to analyse the corrosion resistance for Al, Al-1, Al-2 and Al-3 in 1 M KOH

Table 3 Short-circuit studies of Al-6061 and YSZ-Al alloys

Duration (min)	Al			Al-1			Al-2			Al-3		
	Observed voltage (V)	Observed current (mA)	Current density (mA cm^{-2})	Observed voltage (V)	Observed current (Ma)	Current density (mA cm^{-2})	Observed voltage (V)	Observed current (Ma)	Current density (mA cm^{-2})	Observed voltage (V)	Observed current (mA)	Current density (mA cm^{-2})
0	0.90	50	22.70	1.10	55	25.00	1.20	65.0	29.54	1.30	68.0	30.90
5	0.86	43	19.54	0.95	46	20.90	1.10	57.0	25.90	1.15	60.0	27.21
10	0.80	36	16.36	0.91	40	18.18	0.96	49.0	22.27	0.96	50.0	22.72
15	0.76	35	15.90	0.88	38	17.27	0.91	43.0	19.54	0.91	43.0	19.54
20	0.70	34	15.45	0.86	37	16.81	0.86	38.0	17.27	0.86	39.0	17.72
25	0.68	33.7	15.31	0.84	36	16.36	0.84	38.3	17.40	0.84	38.4	17.45
30	0.61	33.4	15.18	0.79	35	15.90	0.80	38.1	17.31	0.80	38.3	17.40

Table 4 Corrosion parameters derived from IE plots or Tafel Plots

Sample	$^{-}E_{corr}$ (V)	j_{corr}(A cm^{-2})
Al	1.49521	2.25
Al-1	1.50101	2.87
Al-2	1.50899	3.01
Al-3	1.56607	4.12

Table 5 Weight loss of Al electrodes after discharge

Sample name	Weight loss (g)
Al	0.864
Al-1	0.431
Al-2	0.271
Al-3	0.201

electrolyte. In Table 4, LSV measurements are described. It shows the corrosion parameters obtained from potentiodynamic polarization tests. A reduction peak appears at a negative value in Al-3 (ranging from − 1.5 to − 1.6) than Al, Al-1 and Al-2. One of the most common ways to improve anode behaviour is to dope other elements to Al to condense it, thereby making it less corrodible in the electrolyte. While measuring the corrosion characteristics, weight loss during the potentiodynamic test is a very important parameter to consider [48]. Physical retainability after electrochemical functionalities is an important factor for continuous performance and reusability, so the weight loss of the electrode is measured after the completion of electrochemical analysis by the digital weighing balance. The measured weight loss of the Al electrode is given in Table 5.

In the context of corrosion, polarization indicates the shift of potential from the open-circuit potential. The shift in potential can be categorized into anodic and cathodic potentials. If the potential shifts to a more positive region, it is known as anodic polarization, and when it shifts to a more negative region, it is known as cathodic polarization. Cathodic polarization always reduces the rate of corrosion for all metals and alloys in aqueous conditions, accompanied with the formation of a passivation film on the surface of the electrode [49]. In this study, the higher oxidation resistance of Al-1, Al-2 and Al-3 is associated with the alloying of YSZ with Al. The increase in the rate of oxidation resistance could be due to the Zr^{4+} cations, as they react with the growing oxide films on the electrode surface and form pairs with vacancies [50]. The higher YSZ alloying percentage of Al-3 helps a higher number of Zr^{4+} cations react with the oxides; thus, it keeps control over the dissolution of ions to the electrolyte.

The above-mentioned results indicate that the surface corrosion resistance increases at a higher alloying percentage of YSZ in Al. The Tafel plot strongly supports that Al-3 has

higher corrosion resistance than Al, Al-1 and Al-2 alloys. The observed high corrosion resistance strongly helps to increase discharge lifetime and average capacity of the Al–air batteries. The nano-YSZ can be attributed to the high hydrogen over voltage or low exchange current density for hydrogen evolution reaction. In addition, decrease in E_{corr} significantly increases cell life elsewhere [51–54]. The discharge capacity of the Al–air battery is calculated by the following formula [50, 55, 56], and the calculated values are tabulated in Table 2:

$$E = \frac{V_{dvp \cdot q}}{m}, \tag{2}$$

where V_{dvp} is the discharge voltage plateau, q is the charge passing in the reaction and m is the material weight.

The short-circuit study of the Al–air battery used in Al, Al-1, Al-2 and Al-3 in 1 M KOH electrolyte over 0.5 h is shown in Fig. 6. The short-circuit voltages, currents and current densities measured during the short-circuit test are shown in Table 3. The short-circuit voltages for Al, Al-1, Al-2 and Al-3 are 1.11, 1.14, 1.18 and 1.20 V, respectively. The Al-3–air battery exhibits an increase in the current density and open-circuit potential than others, and the current plateau decreases from 68.7 to 39 mA (Fig. 6e).The reduced self-corrosion of the Al-3 anode in the electrolyte reduces the breakdown of the anode.

A comprehensive analysis of the observed results indicates that the distribution of YSZ nanoparticles plays an important role in the Al matrix. With 5% concentration of YSZ in Al-6061, a better crystalline structure arrangement in addition to high corrosion resistance and improved discharge behaviour was obtained in the Al–air battery.

4 Conclusion

A new type of Al–air battery was constructed having three nano-YSZ weight-ratios in Al alloys as electrodes, and their discharge performance was comprehensively analysed. The electrode having a higher weight percentage of nano-YSZ in the Al matrix: namely, Al-3 (YSZ 5 wt. % with Al-6061) demonstrated encouraging discharge behaviour when used as an anode in the Al–air battery compared with the Al-1 and Al-2 electrodes. The SEM, XRD and nano-indentation studies confirmed that Al-3 had the greatest crystallite size and surface hardness than Al, Al-1 and Al-2. The Nyquist plot and Tafel plot for the Al-3 plate exhibited higher corrosion resistance than the Al-1 and Al-2 plates. This shows that Al-3 (YSZ 5% with Al-6061) is a potential candidate for use as an electrode in the Al–air battery.

Acknowledgements S.P. thanks the Second Century Fund: C2F Postdoctoral Fellowship, Chulalongkorn University. The author S.S. expresses their sincere thanks to Dr. R Gopalakrishnan, Principal, K.S. Rangasamy College of Technology (Autonomous), Tiruchengode, India, for their constant support and encouragement to carry out this work.

References

1. Wang N, Wang R, Peng C, Peng B, Feng Y, Hu C (2014) Discharge behaviour of Mg-Al-Pb and Mg-Al-Pb-In alloys as anodes for Mg-air battery. Electrochim Acta 149:193–205
2. Hosseini S, Abbasi A, Uginet L-O, Haustraete N, Praserthdam S, Yonezawa T, Kheawhom S (2019) The influence of dimethyl sulfoxide as electrolyte additive on anodic dissolution of alkaline zinc-air flow battery. Sci Rep 9:14958
3. Teabnamang P, Kao-ian W, Nguyen MT, Yonezawa T, Cheacharoen R, Kheawhom S (2020) High-capacity dual-electrolyte aluminum–air battery with circulating methanol anolyte. Energies 13:2775
4. Phusittananan T, Kao-ian W, Nguyen MT, Yonezawa T, Pornprasertsuk R, Mohamad AA, Kheawhom S (2020) Ethylene glycol/ethanol anolyte for high capacity alkaline aluminum-air battery with dual-electrolyte. Front Energy Res 8:189
5. Siva P, Arunkumar PS, Surendhiran S, Rajendran V (2019) Novel modified nano-activated carbon and its influence on the metal–O2 battery system. J Energy Storage 22:283–294
6. Laoire CO, Mukerjee S, Abraham KM (2010) Influence of nonaqueous solvents on the electrochemistry of oxygen in the rechargeable lithium-air battery. J Phys Chem C 114:9178–9186
7. Girishkumar G, McCloskey B, Luntz AC, Swanson S, Wilcke W (2010) Lithium-air battery: promise and challenges. J Phys Chem Lett 1:2193–2203
8. Rahman Md A, Wang X, Wen C (2013) High energy density metal-air batteries: a review. J Electrochem Soc 160:1759–1771
9. Wang M, Lai Y, Fang J, Li J, Qin F, Zhang K, Lu H (2015) N-doped porous carbon derived from biomass as an advanced electrocatalyst for aqueous aluminium/air battery. Int J Hydrog Energy 40:16230–16237
10. Egan DR, Ponce de León C, Wood RJK, Jones RL, Stokes KR, Walsh FC (2013) Developments in electrode materials and electrolytes for aluminium–air batteries. J Power Sources 236:293–310
11. Revel R, Audichon T, GonzalezS (2014) Non-aqueous aluminium–air battery based on ionic liquid electrolyte. J Power Sources 272:415–421
12. Eftekhari A, Corrochano P (2017) Electrochemical energy storage by aluminum as a lightweight and cheap anode/charge carrier. Sustain energ fuels 1:1246–1264
13. Elia GA, Marquardt K, Hoeppner K, Fantini S, Lin R, Knipping E, Peters W, Drillet J, Passerini S, Hahn R (2016) An Overview and Future Perspectives of Aluminum Batteries. Adv Mater 28:7564–7579
14. Mohamad AA (2008) electrochemical properties of aluminum anodes in gel electrolyte-based aluminum-air batteries. Corros Sci 50:3475–3479
15. Budesk E, Iliev I, Kaisheva A (1989) Investigation of a large capacity medium-power saline aluminium-air battery. J Appl Electrochem 19:323–330
16. Zhang Z, Zuo C, Liu Z, Yu Y, Zuo Y, Song Y (2014) All-solid-state Al air batteries with polymer alkaline gel electrolyte. J Power Sources 251:470–475
17. Hibino T, Kobayashi K, Nagao M (2013) An all solid state rechargeable aluminium air battery with a hydroxide ion conducting Sb(v) doped SnP_2O_7 electrolyte. J Mater Chem A 1:14844–14848

18. Wan Daud WMA, Wan Ali WS (2004) Comparison on pore development of activated carbon produced from palm shell and coconut shell. BioresourTechnol 93:63–69
19. Maria KYC, Wolverton C, Jeffrey PG (2012) First Principles Simulations of the Electrochemical Lithiation and Delithiation of Faceted Crystalline Silicon. J Am Chem Soc 134:35: 14362–14374
20. Ningbo L, Beirong Z, Hongming Z, W X (2015) Effect of carbon content on the structure and electronic properties of silicon oxycarbide anode for lithium ion batteries: a first principle study. J Mater Chem A 3:5067–5071
21. Ningbo L, Beirong Z, Hongming Z, W X (2016) Atomic investigation on reversible lithium storage in amorphous silicon oxycarbide as a high power anode material. J Mater Chem A 4:12328–12333
22. Chia-Yun C, Gyeong SH (2013) Lithiation Behavior of Silicon-Rich Oxide (SiO1/3): A First-Principles Study. Chem Mater 25:3435–3440
23. Shkolnikov E, Zhuk A, Vlaskin M (2011) Aluminum as Energy Carrier: Feasibility Analysis and Current Technologies Overview. Renewable Sustainable Energy Rev 15:4611–4623
24. Migliardini F, Di Palma TM, Gaele MF, Corbo P (2018) Solid and acid electrolytes for Al-air batteries based on xanthan-HCl. hydrogelsJ Solid State Electr 22:2901–2916
25. Wang N, Wang R, Peng C, Peng B, Feng Y, Hu C (2014) Discharge behaviour of Mg-Al-Pb and Mg-Al-Pb-In alloys as anodes for Mg-air battery. Electrochim Acta 28:2274–2286
26. Oghaz MH, Razavi RS, Estark MRL, Ghasemi R (2013) Optimization of morphology and particle size of modified sol gel synthesized YSZ nano powder using Taguchi method. J Nano Res 21:65–70
27. Oghaz MH, Razavi RS, Khajelakzay M (2015) Optimizing sol–gel synthesis of magnesia-stabilized zirconia (MSZ) nanoparticles using Taguchi robust design for thermal barrier coatings (TBCs) applications. J Sol-Gel Sci Technol 73:227–241
28. Oghaz MH, Razavi RS, Estarki MRL (2014) Synthesis and characterization of non-transformable tetragonal YSZ nanopowder by means of Pechini method for thermal barrier coatings (TBCs) applications. J Sol-Gel SciTechnol 70:6–13
29. Oghaz MH, Razavi RS, Ghasemi A (2015) Synthesis and characterization of ceria–yttria co-stabilized zirconia (CYSZ) nanoparticles by sol–gel process for thermal barrier coatings (TBCs). J Sol-Gel Sci Technol 749:603–612
30. Oghaz MH, Razavia RS, Loghmanestarki M (2014) Large-scale synthesis of YSZ nanopowder by Pechini method. Bull Mater Sci 37:5
31. Ariharan S, Gupta A, Keshri A, Agarwa A, Balani K (2012) Size effect of yttria stabilized zirconia addition on fracture toughness and thermal conductivity of plasma sprayed aluminum oxide composite coatings. NanosciNanotechnol 4:3
32. Maridurai T, Balaji, Sagadevan S (2016) Synthesis and characterization of yttrium stabilized zirconia nanoparticles. Mater Res 19:812–816
33. Zhonga XH, Wang YM, Xua ZH, Zhang YF, Zhang JF, Cao Q (2010) Hot-corrosion behaviors of overlay-clad yttria-stabilized zirconia coatings in contact with vanadate–sulfate salts. J Eur Ceram Soc 30:1401–1408
34. Huang W, Cheng H, Zhou Y (2015) Oxidation behavior of plasma-sprayed stabilized zirconia/Al coated polymer matrix composites. RSC Adv 5:72331–72339
35. Estarkia MRL, Razavib RS, Edrisa H, pourbafrany M, Jamalib H, GhasemiR (2014) Life time of new SYSZ thermal barrier coatings produced by plasma spraying method under thermal shock test and high temperature treatment. Ceram Int 40:1405–1414
36. Witz G, Shklover V, Steurer W (2007) Phase evolution in yttria-stabilized zirconia thermal barrier coatings studied by rietveld refinement of X-Ray powder diffraction patterns. J Am Ceram Soc 90:2935–2940
37. Palanisamy S, Srinivasan S, Shyma AP (2019) Influence of nanoflower $FeTiO_3$ in carbon dioxide reduction. SN Appl Sci 1:1230
38. Palanisamy S, Srinivasan S (2019) Electrochemical reduction of CO_2 on Ni $(OH)_2$ doped water dispersible graphene under different electrolyte conditions. SN Appl Sci 1:837
39. Palanisamy S, Shyma AP, Srinivasan S (2019) Water-dispersible graphene–wrapped MnO_2 nanospheres and their applications in coin cell supercapacitors. Ionics 25:4425–4436
40. Estarkia MRL, Oghaz MH, Edrisa H, Razavi RS (2013) Comparative studies on synthesis of nanocrystalline Sc_2O_3–Y_2O_3 doped zirconia (SYDZ) and YSZ solid solution via modified and classic Pechini method. Cryst Eng Comm 15:5898–5909
41. Heshmatpour F, Aghakhanpour RB (2012) Synthesis and characterization of superfine pure tetragonal nanocrystalline sulfated zirconia powder by a non-alkoxide sol–gel route. Adv Powder Technol 23:80–87
42. Dapiaggi M, Maglia F, Tredici I, Maroni B, Borghini G, Tamburini UA (2010) Complex thermal evolution of size-stabilized tetragonal zirconia. J Phys Chem Solids 71:1038–1041
43. Estarkia MRL, Edrisa H, Razavi RS (2013) Large scale synthesis of non-transform able tetragonal Sc_2O_3, Y_2O_3 doped ZrO_2nanopowders via the citric acid based gel method to obtain plasma sprayed coating. Ceram Int 39:7817–7829
44. Mercer C, Williams JR, Clarke DR, Evans AG (2007) On a ferroelastic mechanism governing the toughness of metastable tetragonal-prime (t') yttria-stabilized zirconia. Proc R Soc A 463:1393–1408
45. Feinberg, Perry CH (1981) Structural disorder and phase transitions in ZrO_2YZO_3 system. J Phys Chem Solids 42:513–518
46. Martínez SEH, Cruz-Rivera JJ, Garay-Reyes CG, Elias-Alfaro CG, Martínez-Sánchez R, Hernández-Rivera JL (2015) Application of ball milling in the synthesis of AA 7075–ZrO_2 metal matrix nanocomposite. Powder Technol 284:40–46
47. Guo HX, Lu BT, Luo JL (2006) Response of surface mechanical properties to electrochemical dissolution determined by in situ nanoindentation technique. Electrochem Commun 8:1092–1098
48. Kiroshi K, MakottoK,kenji I (2006) Nanoindentation hardness test for estimation of vickers hardness Transcat JWRI. 35:1
49. Ramachandra M, Dhilip Maruthi G, Rashmi R (2016) Evaluation of corrosion properties of aluminium zirconium dioxide (AlZrO2) nanocomposites. Int Sci Res Innov Innovation 10(10):1321–1326
50. Li Q, Bjerrum NJ (2002) Aluminum as anode for energy storage and conversion: a review. J Power Sources 110:1–10
51. Jirón-Lazos U, Corvo F, De la Rosa SC, García-Ochoa EM, Bastidas DM, Bastidas JM (2018) Localized corrosion of aluminum alloy 6061 in the presence of *Aspergillus niger*. Int BiodeterBiodegr 133:17–25
52. Zaki A (1986) the kinetics of anodic and cathodic polarization of aluminium and its alloys. Anti-Corros Methods Mater 33:4–11
53. Rezaee S, Rasheed G, Golozar MA (2013) Electrochemical and oxidation behavior of yttria stabilized zirconia coating on zircaloy-4 synthesized via sol-gel process. Int J Corros. https://doi.org/10.1155/2013/453835
54. Shuhong J, Jianming Z, Qiuyan L, Xing L, Mark HE, Ruiguo C, Ji-Guang Z, Wu X (2018) Behavior of lithium metal anodes under various capacity utilization and high current density in lithium metal batteries. Joule 2:110–124
55. Yun-Il C, Kalubarme RS, Hee Jin J, Chan-Jin P (2011) Effect of Alloying Elements on the Electrochemical Characteristics of an Al Alloy Electrode for Al-air Batteries in 4 M NaOH solution. Kor J Met Mater 49: 839 ~ 844
56. Mikel P, Carlos C, Joaquí n C, Paloma RG, Enrique F, Pilar O (2014) The electrochemical characteristics of commercial aluminium alloy electrodes for Al/air batteries. J Appl Electrochem 44:1371–1380